The Astrophysical Journal, 882:183 (13pp), 2019 September 10 https://doi.org/10.3847/1538-4357/ab2fe0

Measured Reduction in Alfvén Wave Energy Propagating through Longitudinal Gradients Scaled to Match Solar Coronal Holes

Sayak Bose[1], Troy Carter[2], Michael Hahn[1], Shreekrishna Tripathi[2], Stephen Vincena[2], and Daniel Wolf Savin[1]
[1] Columbia Astrophysics Laboratory, Columbia University, 550 West 120th Street, New York, NY 10027, USA; bose.sayak16@gmail.com
[2] Department of Physics and Astronomy, University of California, Los Angeles, CA 90095, USA
Received 2019 March 27; revised 2019 July 1; accepted 2019 July 4; published 2019 September 16

Abstract

We have explored the effectiveness of a longitudinal gradient in Alfvén speed in reducing the energy of propagating Alfvén waves under conditions scaled to match solar coronal holes. The experiments were conducted in the Large Plasma Device at the University of California, Los Angeles. Our results show that the energy of the transmitted Alfvén wave decreases as the inhomogeneity parameter, λ/L_A, increases. Here, λ is the wavelength of the Alfvén wave and L_A is the scale length of the gradient in Alfvén speed. For gradients similar to those in coronal holes, the waves are observed to lose a factor of $\approx$5 more energy than they do when propagating through a uniform plasma without a gradient. We have carried out further experiments and analyses to constrain the cause of wave energy reduction in the gradient. The loss of Alfvén wave energy from mode coupling is unlikely, as we have not detected any other modes. Contrary to theoretical expectations, the reduction in the energy of the transmitted wave is not accompanied by a detectable reflected wave. Nonlinear effects are ruled out because the amplitude of the initial wave is too small and the wave frequency well below the ion cyclotron frequency. Since the total energy must be conserved, it is possible that the lost wave energy is being deposited in the plasma. Further studies are needed to explore where the energy is going.

Key words: magnetic fields – magnetohydrodynamics (MHD) – plasmas – solar wind – Sun: corona – waves

1. Introduction

Coronal holes are regions of the Sun's atmosphere with open magnetic field lines that extend into interplanetary space. These regions are ~200 times hotter than the underlying photosphere. It is widely established that the fast solar wind originates from coronal holes; but the mechanism responsible for heating coronal holes and accelerating the fast solar wind remains a mystery (Cranmer 2009).

Recent observations at the base of coronal holes have detected Alfvénic waves with sufficient energy to heat coronal holes and accelerate the fast solar wind (McIntosh et al. 2011; Morton et al. 2015). Furthermore, strong damping of Alfvénic waves has been seen at a height of $\approx 0.15\,R_\odot$, where $R_\odot$ is the solar radius, implying that coronal holes are predominantly heated by wave-driven processes (Bemporad & Abbo 2012; Hahn et al. 2012; Hahn & Savin 2013). Here and throughout, all distances in coronal holes are measured from the surface of the Sun. The term Alfvénic is used to highlight that some of the observed waves may not be pure torsional Alfvén waves. Transverse kink waves may also be present (Van Doorsselaere et al. 2008; Goossens et al. 2009, 2012). Studies of chromospheric spicules by De Pontieu et al. (2012) suggest that both modes contribute to the coronal wave energy.

Different models have been put forward to explain the damping of wave energy in coronal holes (Moore et al. 1991a, 1991b; Ofman & Davila 1995; Hood et al. 1997; Matthaeus et al. 1999; Dmitruk et al. 2001; Oughton et al. 2001). A number of these models invoke partial reflection of the upward propagating torsional Alfvén waves (Moore et al. 1991a, 1991b; Matthaeus et al. 1999; Dmitruk et al. 2001; Oughton et al. 2001). This wave reflection is thought to be caused by a strong longitudinal gradient in Alfvén speed along the magnetic field lines at low heights in coronal holes (Moore et al. 1991a; Musielak et al. 1992).

Most of the experiments to date on the propagation of torsional Alfvén waves through a longitudinal gradient in Alfvén speed were motivated by the needs of fusion devices, such as mirror machines. Gradients in Alfvén speed were produced by introducing a non-uniformity in the magnetic field of the machine. Torsional Alfvén waves were excited in the high magnetic field region. These waves propagated along the field lines into a region of decreasing magnetic field to the point where the wave frequency matched the local ion cyclotron frequency, a configuration known as a magnetic beach, causing ion heating. The efficiency of this wave-driven heating was studied in mirror machines (Swanson et al. 1972; Breun et al. 1987; Roberts et al. 1989) using different types of antennas (Stix & Palladino 1958; Yasaka et al. 1988). A few basic plasma physics experiments have also been carried out to study the characteristics of a torsional Alfvén wave through a longitudinal gradient (Vincena et al. 2001; Mitchell et al. 2002). Propagation of Alfvén waves through gradients produced by periodically arranged multiple magnetic wells was studied by Zhang et al. (2008). However, in all the above-mentioned experiments, either the gradient was too weak or the geometry of the gradient was different from that in coronal holes.

Here we report new laboratory experiments to study the propagation of torsional Alfvén waves through a longitudinal gradient in Alfvén speed under conditions scaled to match those of coronal holes. The wave experiments were carried out in the Large Plasma Device (LAPD), located at the University of California, Los Angeles (Gekelman et al. 2016).

The rest of the paper is organized as follows: in Section 2 we describe the basic physics of torsional Alfvén waves and compare the plasma conditions and properties of Alfvén waves in a coronal hole with those in LAPD. The experimental setup is described in Section 3. The results of our wave experiments

are presented in Section 4 and analyzed in Section 5. This is followed by a discussion and summary in Section 6.

2. Alfvén Waves

2.1. Overview

Alfvén waves are one of the fundamental wave modes of magnetized plasmas. These waves were first predicted by Alfvén (1942) using ideal magnetohydrodynamics (MHD). In cylindrical geometry they are commonly referred to as torsional Alfvén waves, while in Cartesian coordinates they are often referred to as shear Alfvén waves. From hereon we will use the term shear Alfvén waves. These waves cause shearing and twisting of magnetic field lines. The resulting magnetic tension provides the restoring force for the waves.

Shear Alfvén waves are low-frequency electromagnetic waves that propagate below the ion cyclotron frequency, $\omega_{ci} = qB_0/m_i$, where q is the ion charge, B_0 is the magnitude of the ambient magnetic field, and m_i is the ion mass. In the ideal MHD limit, these waves transport energy along the ambient magnetic field lines and follow the linear dispersion relation,

$$\omega = v_A k_\parallel. \tag{1}$$

Here, ω is the frequency of the wave in units of rad s^{-1}, v_A is the Alfvén speed, and $k_\parallel$ is the wavenumber parallel to the ambient magnetic field. The Alfvén speed is given by $v_A = B_0/\sqrt{\mu_0 \rho}$, where μ_0 is the permeability of free space, $\rho = n_i m_i + n_e m_e$ is the mass density of the plasma, n_i is the ion number density, n_e is the electron number density, and m_e is the electron mass (Alfvén 1942; Cross 1988; Priest 2014). For quasineutral plasmas, $n_i \simeq n_e \simeq n$, and n is usually referred to as the plasma density.

Shear Alfvén waves interact with the plasma and drive ion and electron currents. Ideal MHD includes the perpendicular motion of the ions in the wave dynamics, but this theory does not explicitly describe the parallel response of electrons. This aspect of shear Alfvén wave dynamics is considered by more advanced theories, such as two-fluid theory, plasma kinetic theory, etc. A commonly used dimensionless parameter to describe the parallel response of an electron is $\bar{\beta} \equiv 2v_{te}^2/(\omega/k_\parallel)^2 \approx 2v_{te}^2/v_A^2$, where $v_{te} = \sqrt{T_e/m_e}$ is the electron thermal velocity and T_e is the electron temperature. In this paper, T_e is expressed in joules in all the formulae unless stated otherwise.

For $\bar{\beta} \gg 1$, the electrons respond adiabatically to the wave field and the wave is called a kinetic Alfvén wave (KAW). The term KAW is also used by some authors for shear Alfvén waves influenced by the ion gyroradius, but we refer specifically to the $\bar{\beta} \gg 1$ regime. The dispersion relation of a KAW is given by (Stasiewicz et al. 2000)

$$\frac{\omega}{k_\parallel} = v_A \sqrt{1 - \bar{\omega}^2(1 + k_\perp^2 \rho_i^2) + k_\perp^2(\rho_s^2 + \rho_i^2)}, \tag{2}$$

where $\bar{\omega} = \omega/\omega_{ci}$, $\rho_i = v_{ti}/\omega_{ci}$ is the ion gyroradius, $v_{ti} = \sqrt{T_i/m_i}$ is the ion thermal velocity, $\rho_s = c_s/\omega_{ci}$ is the ion sound gyroradius, $c_s = \sqrt{T_e/m_i}$ is the ion sound speed, k is the wavenumber, and $\parallel$ and $\perp$ denote the components parallel and perpendicular to the background magnetic field, respectively. The terms $k_\perp^2 \rho_s^2$ and $k_\perp^2 \rho_i^2$ incorporate the effect of the finite perpendicular wavelength into the KAW dispersion relation.

Table 1
Dimensionless Parameters for Coronal Holes and LAPD

Parameter	Coronal Hole	LAPD
$\bar{\beta}$	3–18	1–16
$\bar{\omega}$	$\lesssim 1.5 \times 10^{-5}$	0.3–0.5
$k_\perp^2 \rho_i^2$	$\ll 1$[a]	$\ll 1$
$k_\perp^2 \rho_s^2$	$\ll 1$[a]	$\ll 1$
$(\omega/k_\parallel)/v_A$	1	≈ 1
β_e	$(1.5\text{–}9.6) \times 10^{-3}$	$(0.1\text{–}2.1) \times 10^{-3}$
λ/L_A	$\gtrsim 4.5$	$\approx 0.27\text{–}6.3$
$L_A/\lambda_{mfp,e}$	~ 13	8–20
b/B_0	$\lesssim 0.02$	$\lesssim 8 \times 10^{-5}$

Note.
[a] Based on the assumption that shear Alfvén waves in coronal holes satisfy nearly ideal MHD conditions.

For a typical low-temperature laboratory plasma, T_i is small and $T_e \gg T_i$, resulting in $k_\perp^2 \rho_i^2 \ll 1$ and $k_\perp^2 \rho_s^2 \gg k_\perp^2 \rho_i^2$. Under such conditions, Equation (2) reduces to (Gekelman et al. 1997, 2011)

$$\frac{\omega}{k_\parallel} = v_A \sqrt{1 - \bar{\omega}^2 + k_\perp^2 \rho_s^2}. \tag{3}$$

The term $1 - \bar{\omega}^2$ represents the finite-frequency correction. It causes the parallel phase velocity, $v_{ph,\parallel} = \omega/k_\parallel$, of a shear Alfvén wave to decrease as ω approaches ω_{ci}. When $\bar{\omega}^2 \ll 1$ and $k_\perp^2 \rho_s^2 \ll 1$, the KAW dispersion relation given by Equation (3) reduces to the ideal MHD shear Alfvén wave dispersion relation.

For $\bar{\beta} \ll 1$, the inertia of the electrons becomes important and the wave is called an inertial Alfvén wave (IAW). The dispersion relation of an IAW is given by (Stasiewicz et al. 2000)

$$\frac{\omega}{k_\parallel} = v_A \frac{\sqrt{(1 - \bar{\omega}^2)(1 + k_\perp^2 \rho_i^2)}}{\sqrt{1 + k_\perp^2 \delta^2}}. \tag{4}$$

Here $\delta = c/\omega_{pe}$ is the collisionless electron skin depth, c is the speed of light, and $\omega_{pe} = \sqrt{ne^2/m_e \epsilon_0}$ is the electron plasma frequency, where e is the fundamental unit of electrical charge and ϵ_0 is the permittivity of free space. The IAW dispersion relation reduces to ideal MHD shear Alfvén wave dispersion relation when $\bar{\omega}^2$, $k_\perp^2 \rho_i^2$, and $k_\perp^2 \delta^2$ are all $\ll 1$.

KAWs and IAWs propagate both parallel and perpendicular to the ambient magnetic field with finite parallel and perpendicular group velocities given by $v_{g,\parallel} = \partial\omega/\partial k_\parallel$ and $v_{g,\perp} = \partial\omega/\partial k_\perp$, respectively. Typically, $v_{g,\parallel} \gg v_{g,\perp}$. As a result, energy is transported by these waves predominantly along the magnetic field lines. We also remind the reader that phase velocity refers to velocity of the crest or trough of the wave, while group velocity is the propagation velocity of the total wave envelope.

2.2. Alfvén Waves in Coronal Holes and in LAPD

Shear Alfvén waves are excited by sloshing of the plasma in the photosphere (Narain & Ulmschneider 1996; Priest 2014). They propagate upward through coronal holes along the ambient magnetic field lines. These waves are in the $\bar{\beta} \gg 1$ regime at low heights, and hence are referred to as KAWs. We match this in LAPD in the region where we excite the waves by

setting the parameters such as n, T_e, and B_0 to satisfy the condition $\bar{\beta} \gg 1$ (see Table 1).

In coronal holes, most of the wave energy occurs at $\omega \ll \omega_{ci}$. For example, Morton et al. (2015) reported frequencies $f = \omega/2\pi$ of between 0.2 and 16 mHz. The ambient magnetic field in a coronal hole is ~0.7 G at a height of 0.15 $R_\odot$ (Morton et al. 2015). At this height, $\bar{\omega}$ ranges from $\approx 1.9 \times 10^{-7}$ to 1.5×10^{-5}.

To the best of our knowledge there are no measurements of $k_\perp$ for KAWs in coronal holes. But for the nearly ideal MHD conditions commonly used to model coronal holes, it is typically assumed that both $k_\perp^2\rho_i^2$ and $k_\perp^2\rho_s^2$ are $\ll 1$. As a consequence of $\bar{\omega}^2$, $k_\perp^2\rho_i^2$, and $k_\perp^2\rho_s^2$ all being $\ll 1$, shear Alfvén waves in coronal holes are treated as dispersionless, i.e., their frequency varies as $\omega = v_A k_\parallel$.

We have designed our shear Alfvén wave experiments in LAPD so that $k_\parallel$ varies almost linearly with ω, giving $(\omega/k_\parallel)/v_A \approx 1$. We also excite shear Alfvén waves with dominant perpendicular wavelengths much greater than ρ_i and ρ_s. This ensures that both $k_\perp^2\rho_i^2$ and $k_\perp^2\rho_s^2$ are $\ll 1$. Additionally, we limit the range of $\bar{\omega}$ from 0.3 to 0.5 in order to keep the finite-frequency correction as small as possible.

$T_e \sim T_i$ in coronal holes, whereas $T_e > T_i$ in LAPD. This minor difference does not affect the wave dispersion either in coronal holes or LAPD because the term containing the effect of finite ion temperature in KAW dispersion, $k_\perp^2\rho_i^2$, is negligibly small in both cases.

In coronal holes, magnetic pressure dominates over thermal pressure. This is represented by the dimensionless parameter $\beta_e = 2\mu_0 n T_e / B_0^2$, where μ_0 is the permeability of free space. The value of β_e varies from $\approx 9.6 \times 10^{-3}$ at the surface of the Sun to 1.5×10^{-3} at a height of 0.5 $R_\odot$. To match this in LAPD, we adjusted B_0, n, and T_e to produce a value of β_e ranging from $\approx 2.1 \times 10^{-3}$ where the waves are excited to $\approx 0.1 \times 10^{-3}$ after the v_A gradient.

In coronal holes, the plasma density and magnetic field are highly non-uniform at low heights. This results in a strong spatial inhomogeneity in v_A. The predicted spatial variation is shown in Figure 1. The density and magnetic field used here to calculate v_A are from the approximate fits given by Cranmer & Van Ballegooijen (2005).

For a shear Alfvén wave propagating through a longitudinal gradient in v_A, inhomogeneity-driven effects are predicted to be strong if v_A changes substantially over a single wavelength (Campos 1988; Musielak et al. 1992). Here, the inhomogeneity parameter can be written as λ/L_A, where λ is the wavelength of the shear Alfvén wave and L_A is the minimum scale length of v_A in the gradient. This scale length is defined as v_A/v_A', where v_A' is the first spatial derivative of v_A. The plasma medium is considered to be homogeneous for $\lambda/L_A \ll 1$ and inhomogeneous for $\lambda/L_A \gtrsim 1$.

In coronal holes, L_A is $\approx 0.1\,R_\odot$ (see Figure 1). Alfvénic waves have a broad wavelength spectrum with substantial power in the region of $\lambda \gtrsim 0.45\,R_\odot$ (Morton et al. 2015). As a result, the inhomogeneity parameter in coronal holes is predicted to be $\lambda/L_A \gtrsim 4.5$.

Using LAPD, we have varied λ/L_A from ≈ 0.27 to 6.3. The wavelength of the shear Alfvén wave was increased by reducing the frequency of the excited wave. L_A was controlled by varying the magnetic field gradient in LAPD. We also note that $\lambda/L_A \approx 0.23$ corresponds to wave data acquired in the case of a uniform magnetic field. In a uniform magnetic field and uniform plasma, L_A should be infinite and λ/L_A should be zero. However, in LAPD, there is a weak variation in density along the axis of the machine that gives rise to an even weaker gradient in v_A. This effect produces a large but finite value of L_A that sets the lower limit for the achievable values of λ/L_A. However, this weak background variation in density along LAPD is negligible compared to that due to the magnetic fields applied to generate the v_A gradient, as we show below. Lower values of L_A are achieved by increasing the slope of this applied gradient.

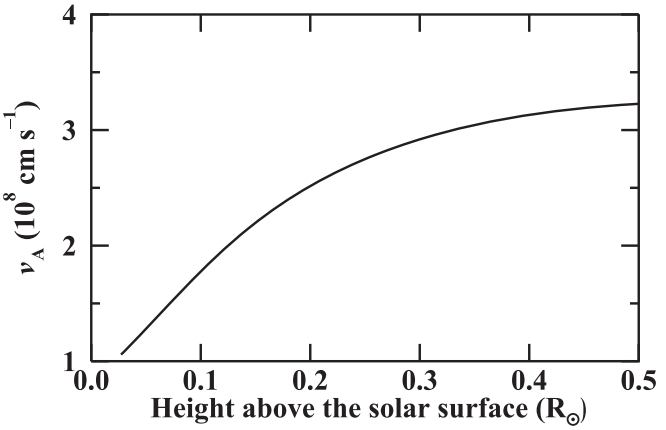

Figure 1. Variation of the Alfvén speed, v_A, in a coronal hole vs. height above the solar surface.

In coronal holes, a consequence of the spatial variation of v_A is that $\bar{\beta}$ also varies with height. The value varies from ≈ 18 at the base of a coronal hole to ≈ 3 at a height of 0.5 $R_\odot$. Thus, shear Alfvén waves are kinetic at low heights; but the waves are expected to exhibit properties between kinetic and inertial with increasing heights. We have mimicked coronal hole conditions in LAPD by exciting the shear Alfvén wave in a region with $\bar{\beta} = 16$. The value of $\bar{\beta}$ then approaches 1 as the wave propagates through the gradient in v_A.

Shear Alfvén waves are also known to be damped by Coulomb collisions (Cramer 2001). This damping is predicted to affect shear Alfvén waves at low heights in coronal holes (Cranmer 2002). The effect of electron–ion collisions on the wave damping in the gradient can be estimated from the ratio of the mean free path of the electrons, $\lambda_{mfp,e}$, to the scale length of the gradient, L_A. This ratio gives a measure of the number of electron mean free paths within the v_A gradient. The value of $\lambda_{mfp,e}$ was calculated using

$$\lambda_{mfp,e} = v_{te}\tau_{ei} = 1.46 \times 10^{11} \frac{T_e^2}{n Z_{ch} \ln\Lambda}, \quad (5)$$

where τ_{ei} is the electron–ion collision time (Braginskii 1965), Z_{ch} is the charge state of the ion, and ln Λ is the Coulomb logarithm (Huba & Naval Research Laboratory 2018). Here, $\lambda_{mfp,e}$ is in meters, for n in cm^{-3} and T_e in eV. For coronal hole conditions of $n \sim 10^7$ cm^{-3} and $T_e \sim 86$ eV (10^6 K) at 0.2 $R_\odot$, we find $\lambda_{mfp,e}$ is $\sim 5.3 \times 10^6$ m $= 0.008\,R_\odot$. Therefore, $L_A/\lambda_{mfp,e} \sim 13$ in coronal holes. In LAPD, we have set the values of n, T_e, and L_A such that $L_A/\lambda_{mfp,e}$ varied from 8 to 20.

Coronal holes extend from the surface of the Sun to interplanetary space, but LAPD is of finite length. However, the magnetic field profile in LAPD is tailored to avoid finite boundary effects. A magnetic beach (Stix 1992) is located

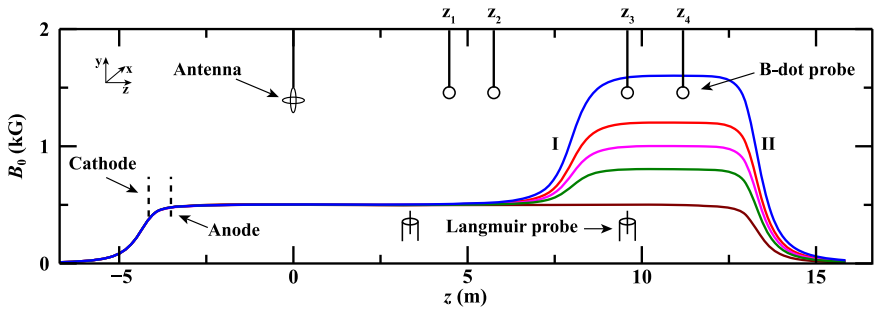

Figure 2. Schematic of the experimental arrangement. The various axial magnetic field profiles used are represented by the different colors. The magnetic field on the low-field side, $B_{\rm lo}$, was set to 500 G for all cases. That on the high-field side, $B_{\rm hi}$, was set to 500 G (maroon), 800 G (green), 1000 G (magenta), 1200 G (red), and 1600 G (blue). The orthogonal ring antenna used to excite shear Alfvén waves is centered on the cylindrical axis of LAPD at $x = y = z = 0$. The vertical ring of the antenna lies in the yz plane, while the horizontal ring lies in the xz plane. The first and second gradients in $v_{\rm A}$ encountered by the excited Alfvén waves are labeled as I and II, respectively. Also shown are the diagnostics that were used to measure the plasma parameters and the wave magnetic field. See the text for additional details.

between the region where we have performed the experiments and the mechanical boundary of LAPD. Shear Alfvén waves are known to be damped very strongly in a magnetic beach due to ion cyclotron resonance, thereby preventing the waves from reaching the mechanical boundary of LAPD. Thus, from the perspective of the wave, LAPD looks infinite.

Lastly, Alfvénic waves in coronal holes have a range of amplitudes depending on ω and $k_{\parallel}$ (Morton et al. 2015). Waves having normalized amplitude as high as $b/B_0 \sim 0.02$ were reported by McIntosh et al. (2011). In LAPD, our experiments were restricted to $b/B_0 \lesssim 8 \times 10^{-5}$. This low-amplitude regime enabled us to avoid known nonlinear effects associated with large-amplitude shear Alfvén waves. In the future, we hope to carry out similar experiments in the large-amplitude regime.

3. Experimental Overview

3.1. Experimental Setup

LAPD houses a 19 m long magnetized plasma column in a cylindrical vacuum chamber of length 24.4 m (Gekelman et al. 2016). The plasma was produced by applying a voltage between a 60 cm diameter hot barium oxide cathode (Leneman et al. 2006) and a mesh anode located 0.5 m away, as shown in Figure 2. Each plasma discharge was pulsed with a 1 Hz repetition rate. The duration of each discharge or shot was ≈10 ms. The experiments were performed in a helium plasma. The neutral helium pressure was held constant at $\sim 10^{-4}$ Torr.

Ten sets of electromagnets are arranged coaxially with the vacuum chamber in order to produce the axial magnetic field. The axial magnetic field points in the $-\hat{z}$ direction for the coordinate system adopted in this paper. We controlled $\lambda/L_{\rm A}$, in part, by creating a gradient in the axial magnetic field. On the low-field side of the machine, we set the magnetic field, $B_{\rm lo}$, to 500 G. $L_{\rm A}$ was varied by setting the field strength on the high-field side, $B_{\rm hi}$, to one of five different values: 500, 800, 1000, 1200, and 1600 G. These magnetic field profiles are shown in Figure 2.

Shear Alfvén waves were excited using an orthogonal ring antenna located on the axis of LAPD at $x = y = z = 0$ (Gigliotti et al. 2009; Karavaev et al. 2011). The diameter of the ring is 9 cm. The dominant perpendicular wavelength, $\lambda_{\perp}$, excited by the orthogonal antenna was typically ∼28 cm. This value of $\lambda_{\perp}$ was determined from the wave data using a Fourier–Bessel analysis (Churchill & Brown 1987) as illustrated by Vincena (1999). In our experiments the dominant $\lambda_{\perp}$ was large enough to ensure that $k_{\perp}^2\rho_{\rm i}^2$, $k_{\perp}^2\rho_{\rm s}^2$, and $k_{\perp}^2\delta^2$ are all $\ll 1$.

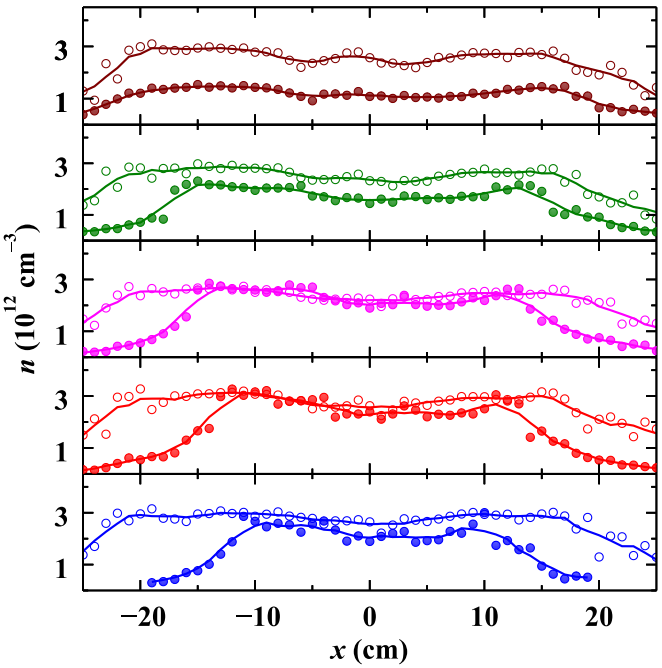

Figure 3. Variation of the plasma density for $y = 0$ along the x axis for the applied axial magnetic field configurations. The different colors represent the magnetic field profiles shown in Figure 2. The open and filled circles show the data acquired by the Langmuir probe before the magnetic field gradient at $z = 3.50$ m and after at 9.59 m, respectively.

The Alfvén wave magnetic fields were measured using triaxial B-dot probes. Each probe consists of three oppositely wound, orthogonally oriented coils. The signals from each pair of coils were amplified using a differential amplifier to avoid electrostatic pickup. The amplified signal was averaged over 14 shots and digitized using a 16 bit data acquisition system. This allows us to detect wave magnetic fields as small as 0.5 mG. The probes are mounted on computer-controlled xy translators that enabled us to map out the wave magnetic field along a cross section of LAPD. The B-dot probes used for most of the measurements reported here were located at axial distances of $z_1 = 4.47$ m, $z_2 = 5.75$ m, $z_3 = 9.59$ m, and $z_4 = 11.18$ m.

3.2. Equilibrium Plasma Parameters

Plasma parameters, such as $T_{\rm e}$ and n, were measured using a Langmuir probe. $T_{\rm e}$ was determined from the slope of the linear region of the $\ln(I_{\rm pr,e})$ versus $V_{\rm pr}$ curve, where $I_{\rm pr,e}$ is the electron

Table 2
Equilibrium Plasma Parameters before and after the Magnetic Field Gradient

Magnetic Field Strength		Before Gradient			After Gradient		
B_{lo} (G)	B_{hi} (G)	n (10^{12} cm^{-3})	T_e (eV)	$\bar{\beta}$	n (10^{12} cm^{-3})	T_e (eV)	$\bar{\beta}$
500	500	2.6 ± 0.3	5.0 ± 0.5	15	1.2 ± 0.2	3.4 ± 0.4	5
500	800	2.6 ± 0.3	5.1 ± 0.5	16	1.8 ± 0.3	3.3 ± 0.5	3
500	1000	2.4 ± 0.2	4.9 ± 0.5	14	2.3 ± 0.3	3.3 ± 0.5	2
500	1200	2.8 ± 0.3	4.9 ± 0.5	16	2.6 ± 0.4	3.2 ± 0.5	2
500	1600	2.8 ± 0.3	4.9 ± 0.5	16	2.3 ± 0.3	3.1 ± 0.5	1

current collected by the probe and V_{pr} is the probe potential. The ion saturation current collected by the probe was used to determine n after calibrating the probe with a heterodyne microwave interferometer.

The variation of n along the x axis in the $y = 0$ plane was measured at $z = 3.50$ m before the gradient and at $z = 9.59$ m after the gradient. Figure 3 shows our measurements for different magnetic field profiles. The uncertainty in each measurement is typically equal to the size of the symbol. Here and throughout the paper, all uncertainties are given at an estimated statistical confidence level of 1σ.

For our analysis of the wave data, we used the spatial average of n over the region sampled by the wave. On the low-field side, at $z = 3.50$ m, this region spans $-20\text{ cm} \leqslant x \leqslant 20$ cm (as shown later in Section 4). On the high-field side, the cross section of the plasma sampled by the Alfvén waves decreases due to the convergence of magnetic field lines. This decreased sample region is determined using the flux conservation equation, $x_{hi} = \sqrt{B_{lo}x_{lo}^2/B_{hi}}$, where $B_{lo} = 500$ G, $x_{lo} = 20$ cm, and B_{hi} is the value of the magnetic field at $z = 9.59$ m. The averaged n and T_e before and after the gradient for different magnetic field configurations are given in Table 2. The ion temperature in LAPD was typically $\sim$1 eV.

4. Results of Wave Experiments

4.1. Excitation of Shear Alfvén Waves

Linearly polarized shear Alfvén waves were excited by applying a sinusoidal wave train of 10 cycles to the horizontal ring of the antenna. The dispersion relation of the excited shear Alfvén wave is shown in Figure 4. The quantity $k_\parallel$ was measured from the phase difference in the wave magnetic field between z_1 and z_2.

The measured value of $k_\parallel$ varies nearly linearly with f for $f \leqslant 0.5 f_{ci}$. Following the predictions of ideal MHD, we have fit a straight line to the data for $f \leqslant 0.5 f_{ci}$. The value of v_A determined from the slope of the fitted line is found to be within 14% of that calculated using n measured with the Langmuir probe. This minor disagreement we attribute to the cumulative uncertainties in the $k_\parallel$ and Langmuir probe measurements.

The theoretical KAW dispersion relation given by Equation (2) is shown by the dashed curve in Figure 4. The value of v_A obtained from the fitted straight line is used to calculate this dashed curve. The measured variation of f with $k_\parallel$ is found to be in good agreement with Equation (2), confirming that the waves excited are indeed KAWs.

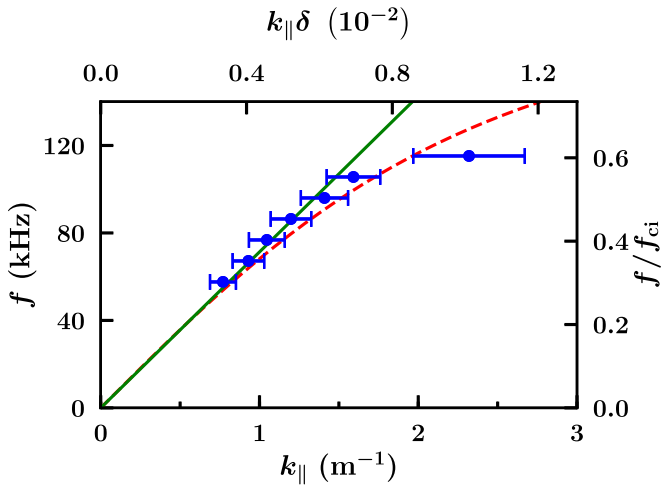

Figure 4. Dispersion relation of the shear Alfvén waves in a uniform 500 G axial magnetic field. The blue symbols represent the experimental data. The green solid and red dashed lines plot the dispersion relation for ideal MHD shear Alfvén waves and for KAWs, respectively. The y axis on the left gives the wave frequency and that on the right shows the wave frequency as a fraction of the ion cyclotron frequency. The lower x axis is the parallel wavenumber while the upper x axis shows the parallel wavenumber in terms of the dimensionless quantity $k_\parallel\delta$.

4.2. Propagation through a Longitudinal Gradient in the Alfvén Speed

4.2.1. Wave Properties before and after the Gradient

The value of $\bar{\beta}$ is $\gg$1 in the low-field region, where the shear Alfvén waves are excited, and decreases to 1 in the high-field region (see Table 2). As a result, the excited shear Alfvén waves do not strictly match the definition of KAWs at all points in space. Hence, we use the more general term shear Alfvén waves to refer to the waves excited by the antenna.

The measured y component of the wave magnetic field is shown in Figure 5 before (a) and after (b) the v_A gradient. The data are shown for $x = y = 0, f = 57.6$ kHz, and $B_{hi} = 1600$ G. Figures 5(c) and (d) show the structure of the shear Alfvén wave on each side of the magnetic field gradient. Two well formed current channels are observed, with the separation between the current channels being smaller on the high-field side of the gradient, as is expected for shear Alfvén waves propagating along converging magnetic field lines.

In order to confirm that the measured property of the shear Alfvén wave is in agreement with the expected theoretical value, we have tried to measure the parallel component of the wave magnetic field, $b_\parallel$, on the axis of LAPD before and after the gradient. According to theory (Hollweg 1999), before the gradient for the dominant $k_\perp \rho_s$ of $\approx$0.21 the predicted value of

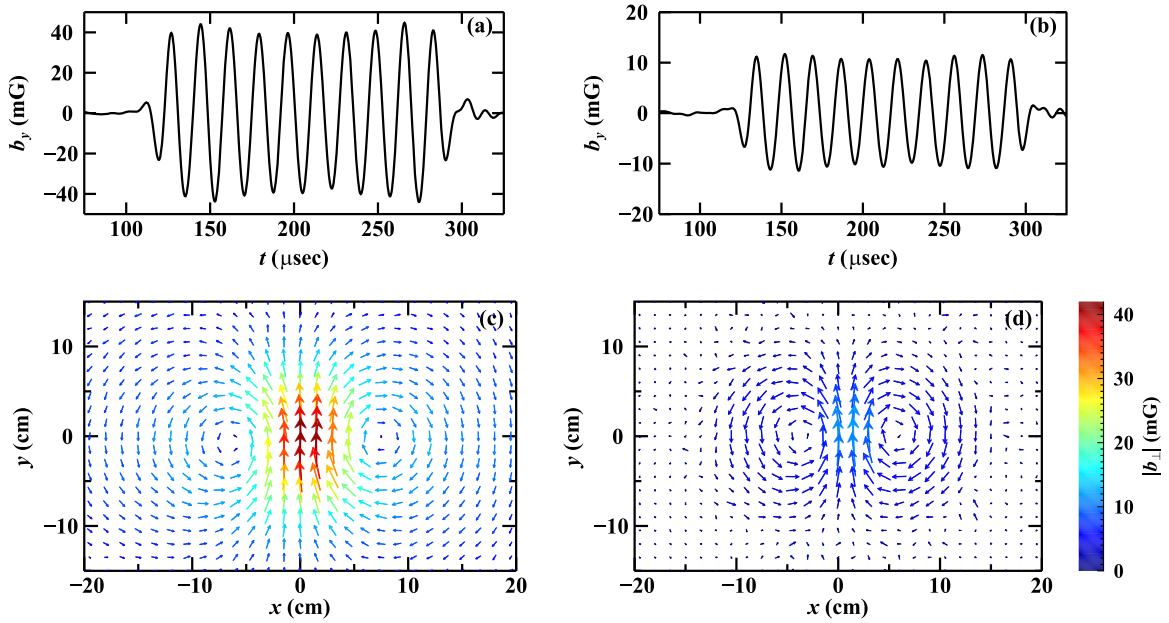

Figure 5. The time variation of the y component of the shear Alfvén wave magnetic field on the axis of LAPD at (a) z_2 and (b) z_4. Also shown are the spatial variation of the wave magnetic vector fields in the xy cross section of LAPD at (c) z_2 and (d) z_4 at times of $t = 161.8$ and 169.2 μs, respectively, corresponding to the third peak of the applied wave train. The direction of the arrows represents that of the wave magnetic field and the colors give the magnitude of the field using the color bar shown. The arrow lengths are normalized by the maximum value of the magnetic field in each panel. For these measurements $B_{\rm lo}$ was held at 500 G and $B_{\rm hi}$ was 1600 G. See text for additional details.

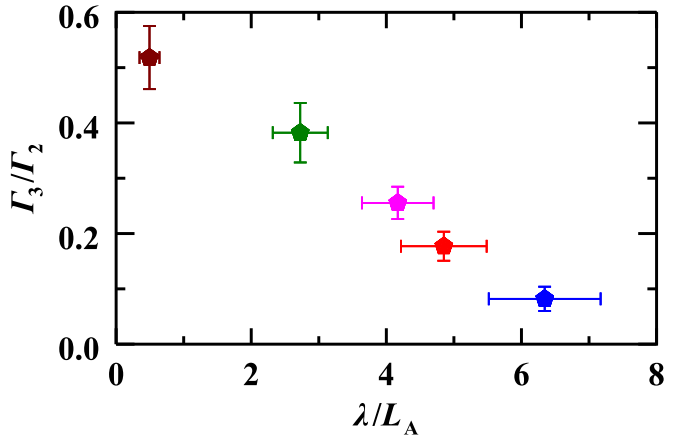

Figure 6. The ratio of the wave powers, Γ_3/Γ_2, passing through the cross section of LAPD at z_3 and z_2, respectively, is shown vs. $\lambda/L_{\rm A}$. $L_{\rm A}$ was varied by increasing the value of $B_{\rm hi}$. The different colors indicate the different values of $B_{\rm hi}$ as given in Figure 2. The wave frequency was held constant at 57.6 kHz.

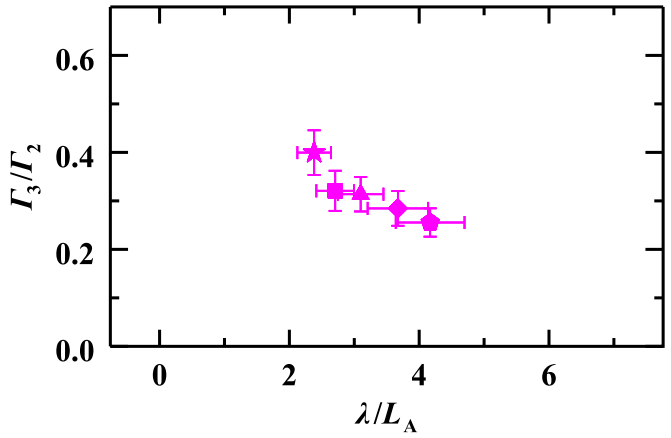

Figure 7. Same as Figure 6, but here $\lambda/L_{\rm A}$ was varied by changing λ, while $L_{\rm A}$ was kept fixed with $B_{\rm hi} = 1000$ G. Results are shown for $f = 57.6$ kHz (pentagon), 67.2 kHz (diamond), 76.8 kHz (triangle), 86.4 kHz (square), and 96.0 kHz (star).

$b_\parallel$ is ≈0.22 mG, while after the gradient for the dominant $k_\perp \rho_s$ of ≈0.08 the predicted value of $b_\parallel$ is ≈0.01 mG. These values of $b_\parallel$ are below our measurement threshold of 0.5 mG. Therefore, the lack of detection of $b_\parallel$ is consistent with the theoretical prediction.

4.2.2. Determination of Wave Energy

The energy of the shear Alfvén wave is obtained using the Poynting vector, S, crossing a plane perpendicular to the ambient magnetic field. This is given by (Karavaev et al. 2011)

$$S = \frac{1}{\mu_0} b^2 v_{\rm g,\parallel} = \frac{1}{\mu_0} b^2 v_{\rm ph,\parallel}. \quad (6)$$

S is the energy flux. In Equation (6), $v_{\rm g,\parallel}$ is considered to be equal to $v_{\rm ph,\parallel}$ because the experiments are limited to $\omega \leqslant 0.5\omega_{\rm ci}$, where the dispersion relation for shear Alfvén waves is nearly linear. Hence, the total wave energy, $\mathcal{E}$, passing through the cross section of LAPD perpendicular to the ambient magnetic field can be expressed as

$$\mathcal{E} = \int \left(\iint S \, dx \, dy \right) dt = \frac{v_{\rm ph,\parallel}}{4\pi} \int \left(\iint b^2 \, dx \, dy \right) dt. \quad (7)$$

The spatial integration is carried out over the cross section of LAPD and the integration in time is carried out over the duration of the wave train, examples of which are shown in Figure 5. The wave power, Γ, is related to the total wave

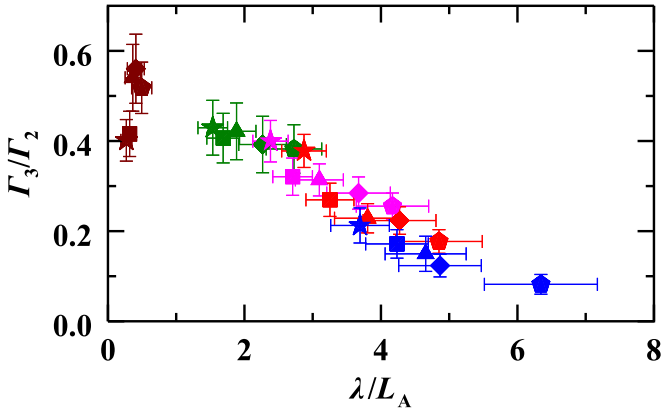

Figure 8. Γ_3/Γ_2 vs. λ/L_A when either λ or L_A is varied. The colors and symbols are defined in Figures 2 and 7, respectively. The plotted data are also given in Table 3.

energy by the relation

$$\Gamma = \frac{E}{t_{dur}}, \tag{8}$$

where t_{dur} is the duration of the wave train. The value of $v_{ph,\parallel}$ used in Equation (7) was determined by simultaneously measuring the wave magnetic field using two axially separated B-dot probes. The probes were carefully aligned to ensure that both intersected the same axial magnetic field line. To calculate $v_{ph,\parallel}$, the axial distance between the probes was divided by the time lag between the phases of the wave magnetic field. The time lag was determined by a cross-correlation analysis of the time variation of the data acquired by the two probes. The probes located at z_1 and z_2 were used to measure $v_{ph,\parallel}$ on the low-field side, while the probes located at z_3 and z_4 were used to measure $v_{ph,\parallel}$ on the high-field side.

4.2.3. Reduction in Power of the Transmitted Alfvén Wave

The reduction in power of the wave propagating through the gradient was measured using the ratio of the transmitted wave power Γ_3 at z_3 to the incident wave power Γ_2 at z_2. Since Γ is related to $\mathcal{E}$ by a constant factor, the reduction in wave power is equal to the decrease in wave energy, i.e., $\Gamma_3/\Gamma_2 = E_3/E_2$. The dependence of Γ_3/Γ_2 on λ/L_A was studied by varying λ/L_A in two ways. In the first set of experiments, L_A was changed while holding λ constant. In the second set, λ was varied and L_A was kept constant.

For the first set of experiments, the values of L_A were varied by increasing B_{hi} from 500 G to 800, 1000, 1200, and 1600 G. The increase in the value of B_{hi} enhances the steepness of the gradient in v_A. This, in turn, decreases L_A.

The variation of Γ_3/Γ_2 with λ/L_A while varying L_A is shown in Figure 6. Waves of frequency $f = 57.6$ kHz were excited to keep λ fixed. For the nearly homogeneous case of $\lambda/L_A \approx 0.49$, we find $\Gamma_3/\Gamma_2 \approx 0.52$. For a large non-uniformity of $\lambda/L_A \approx 6.3$, we find $\Gamma_3/\Gamma_2 \approx 0.08$. These results show that the wave power propagating through the gradient decreases as the steepness of the gradient increases.

In the second set of measurements, λ was varied by changing f from 57.6 to 96 kHz in steps of 9.6 kHz. We confined f to this range so that the shear Alfvén waves followed the linear dispersion relation to a good approximation. L_A was kept fixed by setting $B_{hi} = 1000$ G. Figure 7 shows that Γ_3/Γ_2 decreases with increasing λ/L_A while varying λ. For example, $\Gamma_3/\Gamma_2 \approx 0.40$ for $\lambda/L_A \approx 2.38$, while $\Gamma_3/\Gamma_2 \approx 0.26$ for $\lambda/L_A \approx 4.17$. This shows that a wave with a longer wavelength loses more energy than one with a shorter wavelength while propagating through a constant gradient.

The decrease in Γ_3/Γ_2 with increasing λ/L_A presented in Figure 7 shows the same quantitative behavior as seen in Figure 6. This confirms that it is neither λ nor L_A but rather λ/L_A that is the independent parameter describing the effect of inhomogeneity on the shear Alfvén waves.

The variation of Γ_3/Γ_2 for all measured values of λ/L_A is shown in Figure 8 and given in Table 3. Here, λ/L_A was varied by changing f from 57.6 to 96 kHz for each of the five values of B_{hi} given in Figure 2. The data in Figure 8 include all of the data plotted in Figures 6 and 7, as well as the additional values listed in Table 3 but not included in Figures 6 and 7.

The $B_{hi} = 500$ G data points in Figure 8 correspond to the case of a flat magnetic field, where the inhomogeneity in v_A is small with $\lambda/L_A < 0.5$. $\Gamma_3/\Gamma_2 \approx 0.54$ for the three lower frequency measurements and $\approx$0.41 for the two higher frequencies. The vertical error bars for all five frequencies nearly overlap. We attribute these minor differences to damping mechanisms that are most readily observable in a uniform plasma. No such similar differences versus frequency were seen in our gradient-driven results, which show an almost monotonic reduction in Γ_3/Γ_2 with increasing λ/L_A. For the gradient cases, the observed energy reduction relative to the non-gradient cases is substantial, with a decrease by a factor of $\approx$5. Moreover, the monotonic nature of the decrease strongly suggests that the energy reduction is due to a gradient-driven effect.

Table 3
Γ_3/Γ_2 vs. λ/L_A

B_{hi} (G)	f (kHz)	λ/L_A	Γ_3/Γ_2
500	57.6	0.49 ± 0.15	0.52 ± 0.06
500	67.2	0.41 ± 0.12	0.56 ± 0.08
500	76.8	0.36 ± 0.11	0.54 ± 0.07
500	86.4	0.32 ± 0.10	0.42 ± 0.05
500	96.0	0.27 ± 0.08	0.40 ± 0.05
800	57.6	2.73 ± 0.41	0.38 ± 0.05
800	67.2	2.27 ± 0.35	0.39 ± 0.06
800	76.8	1.88 ± 0.28	0.42 ± 0.06
800	86.4	1.69 ± 0.24	0.41 ± 0.05
800	96.0	1.54 ± 0.22	0.43 ± 0.06
1000	57.6	4.17 ± 0.53	0.26 ± 0.03
1000	67.2	3.67 ± 0.47	0.28 ± 0.04
1000	76.8	3.10 ± 0.35	0.31 ± 0.04
1000	86.4	2.71 ± 0.29	0.32 ± 0.04
1000	96.0	2.38 ± 0.26	0.40 ± 0.05
1200	57.6	4.85 ± 0.64	0.18 ± 0.03
1200	67.2	4.27 ± 0.53	0.22 ± 0.03
1200	76.8	3.80 ± 0.49	0.23 ± 0.03
1200	86.4	3.25 ± 0.35	0.27 ± 0.04
1200	96.0	2.87 ± 0.33	0.38 ± 0.05
1600	57.6	6.34 ± 0.83	0.08 ± 0.02
1600	67.2	4.87 ± 0.61	0.12 ± 0.03
1600	76.8	4.66 ± 0.59	0.15 ± 0.04
1600	86.4	4.24 ± 0.46	0.17 ± 0.03
1600	96.0	3.69 ± 0.43	0.21 ± 0.04

5. Analysis

In this section we first develop a model for the damping of shear Alfvén waves in a uniform magnetic field in order to understand the reduction in wave energy for the homogeneous case. We then move on to explore the cause of the observed reduction in energy of waves propagating through a v_A gradient for the inhomogeneous case.

5.1. Reduction of Wave Energy in a Uniform Magnetic Field

The flat-field data in Figure 8 show that shear Alfvén waves are damped in LAPD while propagating in a uniform 500 G magnetic field. Shear Alfvén waves propagating in a uniform plasma are known to lose energy due to Landau damping and collisions (Cramer 2001). Below we present numerical calculations quantifying the contribution of these two processes to the observed wave energy reduction.

5.1.1. Antenna Model

The two-dimensional structure of the wave magnetic field in Figure 5 suggests that the ring antenna was in effect was driving two counterpropagating current channels along the axial magnetic field lines of LAPD. Field-aligned time-varying currents with frequencies below f_{ci} are known to radiate shear Alfvén waves (Morales et al. 1994; Gekelman et al. 1994; Morales & Maggs 1997). Hence, we have modeled the antenna as two current sources driving field-aligned currents that are 180° out of phase with one another.

More specifically, the ring antenna located at $x = y = z = 0$ is modeled as two disks separated by a distance equal to the diameter of the ring, which is ≈9 cm. The current density across the surface of each disk is assumed to have a Gaussian profile, $j_0 \exp[-r^2/a^2]$, where j_0 is the amplitude of the surface current density, r is radial the distance from the center of the disk, and a is a measure of the width of the current source. The wave magnetic field due to each current source lies in the azimuthal plane. This azimuthal wave magnetic field, b_ϕ, due to each disk is given by (Morales & Maggs 1997; Vincena 1999)

$$b_\phi = \frac{2j_0\pi a^2}{c}\int_0^\infty \exp\left[-\frac{a^2k_\perp^2}{4}\right]J_1(k_\perp r)\exp\left[ik_\parallel(k_\perp)z\right]dk_\perp. \tag{9}$$

Here, z is the axial distance from the antenna at which the wave magnetic field is calculated, $i = \sqrt{-1}$, J_1 is the Bessel function of the first kind of order one, and $k_\parallel = k_{r,\parallel} + ik_{i,\parallel}$ is a complex quantity where the real and imaginary parts are inversely proportional to the wavelength and damping length, respectively. Note that $k_\parallel$ is a complex quantity only in the formulas mentioned here in Section 5.1. In all other sections and subsections in this paper, $k_\parallel$ is a real quantity as defined in Section 2.

In order to simplify the calculation, we have normalized b_ϕ by the constant factor $2j_0\pi a^2/c$ to obtain

$$b_{\phi,n} = \frac{b_\phi c}{2j_0\pi a^2}. \tag{10}$$

The sole purpose of developing this model is to determine the damping length of the wave energy, which depends on the relative decrease in wave energy versus the distance from the antenna. Our results for damping length are not affected by this normalization.

5.1.2. Landau and Collisional Damping

Landau damping is described by the warm plasma collisionless dispersion relation of shear Alfvén waves derived from the linearized Vlasov equation and Maxwell's equations (Swanson 1989). This relation is given by (Stasiewicz et al. 2000; Lysak 2008; Thuecks et al. 2009)

$$Z'(\xi)\left[\frac{v_A^2}{2v_{te}^2}\frac{(1-\bar{\omega}^2)\mu_i}{1-\Gamma_0(\mu_i)} - \xi^2\right] = k_\perp^2\delta^2, \tag{11}$$

where $\xi = \omega/(\sqrt{2}k_\parallel v_{te})$, $Z'(\xi) = -2\{1 + \xi Z(\xi)\}$ is the derivative of the plasma dispersion function, Z, (Fried & Conte 1961) with respect to ξ, $\mu_i = k_\perp^2\rho_i^2$, $\rho_i = m_i v_{ti}/qB_0$ is the ion gyroradius, $\Gamma_0(\mu_i) = e^{-\mu_i}I_0(\mu_i)$, and I_0 is the modified Bessel function of order zero.

Collisional damping is modeled in the wave dispersion by including the Krook collision operator in the linearized Vlasov equation (Gross 1951; Swanson 1989). The resulting dispersion relation is given by (Gekelman et al. 1997; Thuecks et al. 2009)

$$Z'(\eta)\left(1 + i\frac{\nu_e}{\omega}\right)\left[\frac{v_A^2}{2v_{te}^2}\frac{(1-\bar{\omega}^2)\mu_i}{1-\Gamma_0(\mu_i)} - \xi^2\right] = k_\perp^2\delta^2, \tag{12}$$

where $\eta = \xi(1 + i\nu_e/\omega)$ and ν_e is the collision frequency for electrons. The collision frequency is $\nu_e = \nu_{ei} + \nu_{en}$, where ν_{ei} and ν_{en} are the electron–ion and electron–neutral collision frequencies, respectively. From this dispersion relation we determine $k_\parallel$ as a function of $k_\perp$, which we then substitute into Equation (10) to include the effect of Landau and collisional damping in the model.

The electron–ion collision frequency is calculated in units of hertz using the expression (Braginskii 1965)

$$\nu_{ei} = 2.9 \times 10^{-6}\frac{Z_{ch}n\ln\Lambda}{T_e^{3/2}}, \tag{13}$$

where n is in cm^{-3} and T_e is in eV. The electron–neutral collision frequency is determined using the formula given by Baille et al. (1981). For our experimental parameters of $n = 2.6 \times 10^{12}\,cm^{-3}$, neutral pressure of 10^{-4} Torr, and $T_e = 5$ eV in a He^+ plasma, $\nu_{ei} \approx 7.5 \times 10^6$ Hz and $\nu_{en} \approx 4 \times 10^5$ Hz.

Equation (12) gives the dispersion relation of shear Alfvén waves in the presence of Landau and collisional damping. In order to determine the damping due to collisions only, we have used the collisional dispersion relation of shear Alfvén waves derived using the two-fluid theory in the $\bar{\beta} \gg 1$ limit (Vranjes et al. 2006; Gigliotti et al. 2009),

$$\omega^2 - k_\parallel^2 v_A^2(1 - \bar{\omega}^2 + k_\perp^2\rho_s^2) + i\omega k_\perp^2\delta^2\nu_e = 0. \tag{14}$$

This two-fluid dispersion relation can be solved algebraically, where $k_{r,\parallel}$ and $k_{i,\parallel}$ are given by

$$k_{r,\parallel} = \frac{1}{\sqrt{2}}\frac{\omega}{v_A}\left[\frac{\sqrt{1 + k_\perp^4\delta^4(\nu_e/\omega)^2} + 1}{1 - \bar{\omega}^2 + k_\perp^2\rho_s^2}\right]^{1/2}, \tag{15}$$

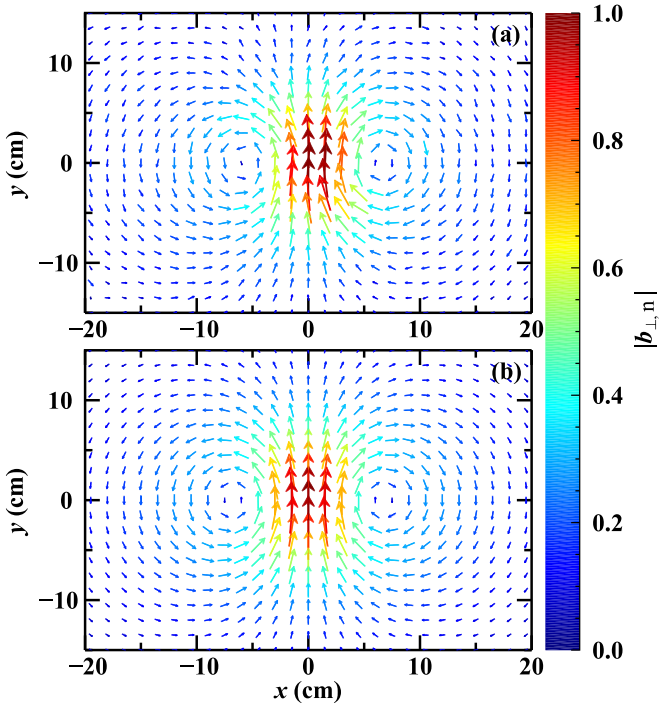

Figure 9. Comparison of the two-dimensional wave structure of a 57.6 kHz shear Alfvén wave at z_2 in a uniform 500 G magnetic field: (a) as measured by the B-dot probe and (b) as predicted by the antenna and wave propagation model. See the text for additional details.

$$k_{i,\parallel} = \frac{1}{\sqrt{2}}\frac{\omega}{v_A}\left[\frac{\sqrt{1 + k_\perp^4\delta^4(\nu_e/\omega)^2} - 1}{1 - \bar{\omega}^2 + k_\perp^2\rho_s^2}\right]^{1/2}. \quad (16)$$

Using Equations (15) and (16), we have determined $k_\parallel$ as a function of $k_\perp$, and substituted $k_\parallel(k_\perp)$ in Equation (10) to include the effect of only collisional damping in the model.

5.1.3. Wave Propagation Model

In order to compare the structure of the experimentally measured wave magnetic field with that predicted by the model we first calculated b_ϕ in a cylindrical coordinate system due to each current source using Equation (10). The value of b_ϕ for each source is then converted from the cylindrical coordinates to Cartesian coordinates as $b_\phi = b_x\hat{x} + b_y\hat{y}$. The total wave magnetic field produced by the ring antenna can then be modeled by a linear superposition of $b_x\hat{x} + b_y\hat{y}$ produced by the two disk sources. We refer to this total wave magnetic field as $b_\perp$.

The experimentally measured $b_\perp$ is compared in Figure 9 to the field calculated at z_2 for $B_0 = 500$ G and $f = 57.6$ kHz. The measured and calculated $b_\perp$, normalized by their maximum values, are denoted as $b_{\perp,n}$. In the antenna model we set $a = 0.25$ cm, which is the thickness of the ring antenna. The average values of n and T_e given in Table 2 were used for the numerical calculation. Figure 9 shows the wave structure predicted by the model using Equation (12). This structure is in excellent agreement with the measured wave magnetic field. The difference in the total wave energy, Γ, in the xy plane calculated from the experimental and numerical data is typically ~4%.

The damping of wave energy in the model was determined by calculating Equation (10) at multiple z locations along the LAPD axis. Figure 10 presents the calculated damping of the shear Alfvén wave shown in Figure 9. The energy decay follows an exponential curve to a good approximation. The damping length, d, is obtained by fitting a function of the form $A\exp[-z/d]$ to the numerically calculated data, where A is a constant.

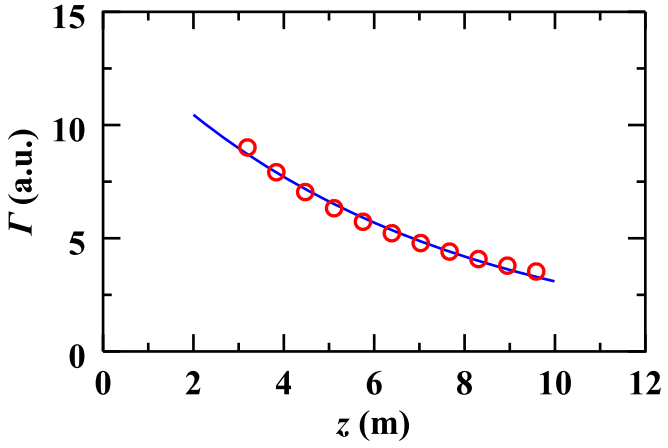

Figure 10. Damping of the modeled shear Alfvén wave energy vs. distance along the LAPD axis. The wave energy values calculated using the model are given by red circles. The blue line is obtained by fitting a function of the form $A\exp[-z/d]$.

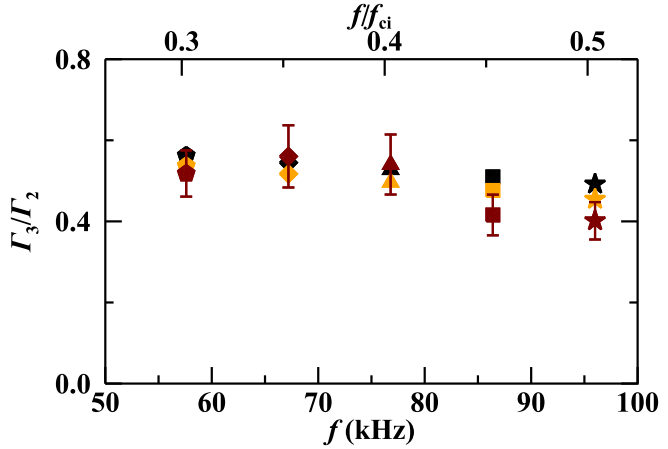

Figure 11. Comparison of the experimentally measured reduction in wave energy, Γ_3/Γ_2, between z_2 and z_3 and the theoretically calculated decrease in wave energy, using the antenna wave propagation model for $B_{lo} = B_{hi} = 500$ G. The maroon symbols represent the experimental data. The black and orange symbols respectively represent the energy reduction due to collisional damping only and due to the combined effects of Landau and collisional damping.

The reason that the energy damping curve of the shear Alfvén wave approximately follows an exponential curve may be understood as follows. The wave magnetic field is obtained by integrating over a number of $k_\perp$ as discussed by Morales & Maggs (1997). For a shear Alfvén wave of a given frequency, different values of $k_\perp$ have different damping lengths as shown by Gekelman et al. (1997), Kletzing et al. (2003), and Lysak (2008). The cumulative effect of these multiple $k_\perp$ results in the energy decay being approximately exponential.

The measured and modeled results for Γ_3/Γ_2 are shown in Figure 11. The errors in the numerically calculated data were determined using a Monte Carlo method, by considering the uncertainties in n and T_e given in Table 2, and are of the order of the size of the plotted symbols.

Comparing our observed damping for the flat 500 G case to our model results, we find that the reduction in wave energy predicted by the model by considering both Landau and collisional damping is in good agreement with the experiment. The comparison shown in Figure 11 of the modeled results due to Landau and collisional damping, and to collisional damping alone, shows that collisional damping is dominant. Landau damping, while present, is very weak.

5.2. Reduction of Wave Energy in the Gradient

5.2.1. Wave Reflection

Light and other electromagnetic waves undergo reflection while propagating across a change in refractive index, corresponding to a change in the propagation velocity of the wave. Similarly, according to both theoretical studies and numerical simulations, shear Alfvén waves propagating through a strong longitudinal v_A gradient are predicted to undergo reflection (Moore et al. 1991a; Musielak et al. 1992; Perez & Chandran 2013).

According to the theory of Musielak et al. (1992), a shear Alfvén wave incident on a longitudinal v_A gradient is expected to undergo strong reflection when the frequency of the wave is less than the critical frequency f_{cr} given by

$$f_{cr} = \frac{1}{2}\sqrt{(v_A')^2 + |2v_A v_A''|}. \quad (17)$$

Here, the double prime indicates the second spatial derivative. This expression was deduced for gradients in n and B_0 in one dimension.

In the wave experiments described in Section 4.2, the shear Alfvén waves passes through two gradients in v_A, labeled as I and II in Figure 2. The difference between these gradients is that v_A increases with distance in gradient I, while it decreases with distance in gradient II. In order to constrain the role of reflected waves in the observed reduction in the transmitted wave energy versus λ/L_A, we performed several measurements to measure the magnitude of any reflected waves.

The first two sets of wave-reflection experiments were carried out to search for reflection from gradient I. B-dot probes were positioned at z_1 and z_2 as indicated in Figure 12. Shear Alfvén waves were excited by applying a sinusoidal wave train of two cycles to the antenna. This reduced the temporal length of the wave train compared to the previously excited ten-cycle wave train. The gradient was also moved to the far end of the machine, as shown in Figure 12. This ensured that the time required for a wave to traverse the distance from the B-dot probe at z_1 to gradient I and return to z_1 was greater than twice the time period of the lowest wave frequency investigated. As a result, the incident wave and any reflected wave would be separated in time in the B-dot probe data. Lastly, the range of frequencies was selected to satisfy the criteria: (a) the wave was predicted to be strongly reflected by theory and (b) there was an overlap in the values of λ/L_A with the inhomogeneity observed in coronal holes of $\lambda/L_A \gtrsim 4.5$.

The magnetic field profile used in the first set of wave-reflection experiments is shown by the solid curve in Figure 12. This curve was obtained by increasing B_{hi} to ≈1382 G. The value of f_{cr} varied axially with the magnetic field variation and reached a maximum value of ≈724 kHz at $z = 12.14$ m within gradient I. In order to satisfy the theoretical criteria for strong reflection we excited wave frequencies below 724 kHz.

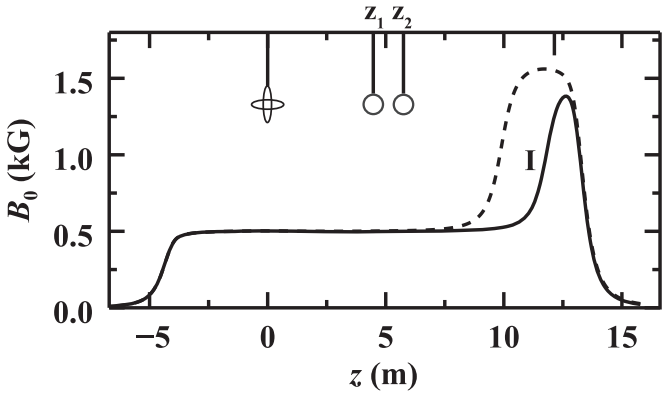

Figure 12. Magnetic field profile used for studying reflection of wave energy from the v_A gradient labeled as I. The locations z_1 and z_2 are the same as in Figure 2.

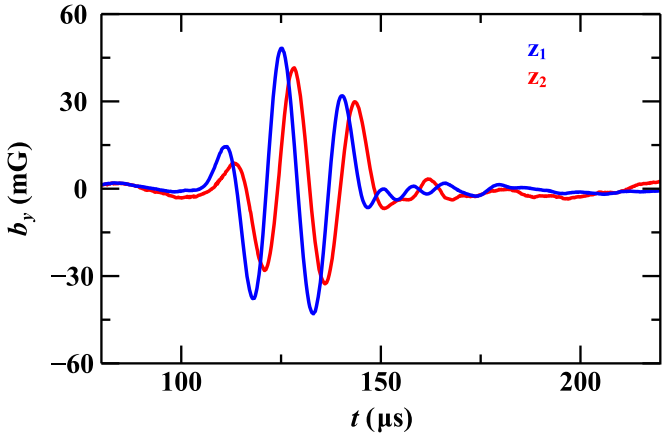

Figure 13. Time variation of b_y as measured on the axis of LAPD at z_1 and z_2 for $f = 65$ kHz. The magnetic field profile corresponding to these wave data is given by the solid line in Figure 12.

Figure 13 shows the y component of the wave magnetic field detected for $f = 65$ kHz (i.e., $f/f_{cr} = 0.09$). A well formed two-cycle incident wave was detected by probes at z_1 and z_2 between ≈112 and 148 μs. For this wave $\lambda/L_A \approx 5.6$. If the shear Alfvén wave were strongly reflected by gradient I, then the reflected wave would reach z_1 at 39 μs after the incident wave has passed it. Hence, a reflected wave is predicted to be observed in Figure 13 between ≈151 and 187 μs. However, we do not observe any reflected wave in this time window. The wave signal at z_1 always leads the signal at z_2, implying that the B-dot probes did not detect any waves reflected by gradient I. We also find no detectable reflected wave in the b_x and b_z directions

There are some small-amplitude fluctuations trailing the applied two-cycle wave train, but these features have a frequency twice that of the applied waveform. We believe that these are excited by the second harmonic present in the antenna signal and are unrelated to reflection from gradient I.

We have also considered the possibility that waves did not reflect exactly along the axis, but found no evidence for reflected waves at any location in the LAPD cross section. The B-dot probes were scanned through a cross section in LAPD and the results were always similar to those shown in Figure 13.

We repeated all of these measurements while increasing f to 190 kHz in steps of 5 kHz. This caused f/f_{cr} to increase to 0.3.

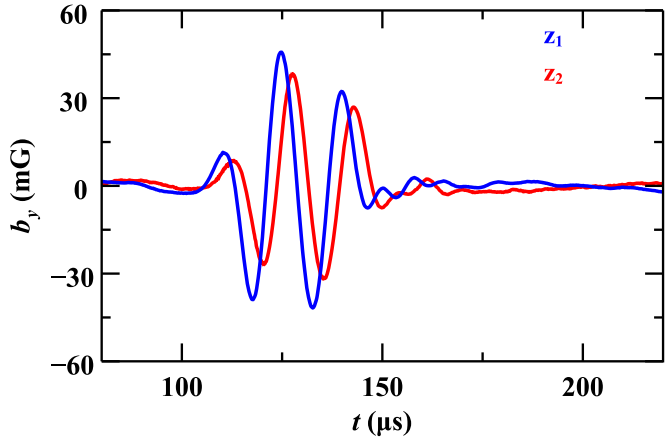

Figure 14. Same as Figure 13 but for $B_{lo} = B_{hi} = 500$ G.

As before, we did not observe a detectable reflected wave at any of the measured frequencies.

We then carried out a second set of experiments to study the possible effects of tunneling through the high v_A region. For the above wave-reflection studies, λ was greater than the width, w, of the high-field region. For example, $\lambda/w \approx 2.1$ for $f/f_{cr} = 0.1$. To rule out the possibility that the shear Alfvén wave could be tunneling through the high v_A region, instead of undergoing reflection, we moved gradient I closer to the antenna, as represented by the dashed line in Figure 12. This resulted in $\lambda/w \approx 1.1$. We then repeated the wave-reflection experiments described above and again did not observe any detectable reflected waves.

The lack of an observable reflected wave from gradient I may imply that the amplitude of the reflected wave is too weak to be detected. For example, using the measured initial wave amplitude at z_1 and taking into account Landau and collisional damping as the wave propagates from z_1 to gradient I and back, we estimate that if there were 100% reflection at gradient I then we would measure a reflected wave signal at z_1 with an amplitude of 11 mG. This is much larger than the ≈1.5 mG fluctuations in Figure 13 trailing the applied two-cycle wave train and should be readily observable. The lack of an observed reflected signal indicates that the efficiency of any reflection by the gradient is much less than 100%. Taking 3 mG as a reasonable detectable level over the 1.5 mG fluctuations trailing the applied wave train, and taking into account Landau and collisional damping between z_1 and gradient I and back to z_1, we can put an upper limit on the reflected wave energy of ≈7.4% for $\lambda/L_A \approx 5.6$ and $f/f_{cr} = 0.09$. This reflectance is too small to account for the observed loss of wave energy.

Finally, in the third set of wave-reflection experiments, we investigated the effects of gradient II. For this we set $B_{lo} = B_{hi} = 500$ G, the flat-field case shown in Figure 2. Here, f_{cr} had a maximum value of ≈364 kHz within gradient II at $z = 13$ m. As before, shear Alfvén waves were excited by applying a sinusoidal wave train comprising two cycles to the antenna located at $z = 0$. The corresponding variation of b_y at z_1 and z_2 for $f = 65$ kHz is shown in Figure 14. Similar to the results from the first two sets of wave-reflection measurements, the phase of the wave signal at z_1 always leads the wave signal at z_2, indicating that the B-dot probes did not detect any reflection from the gradient.

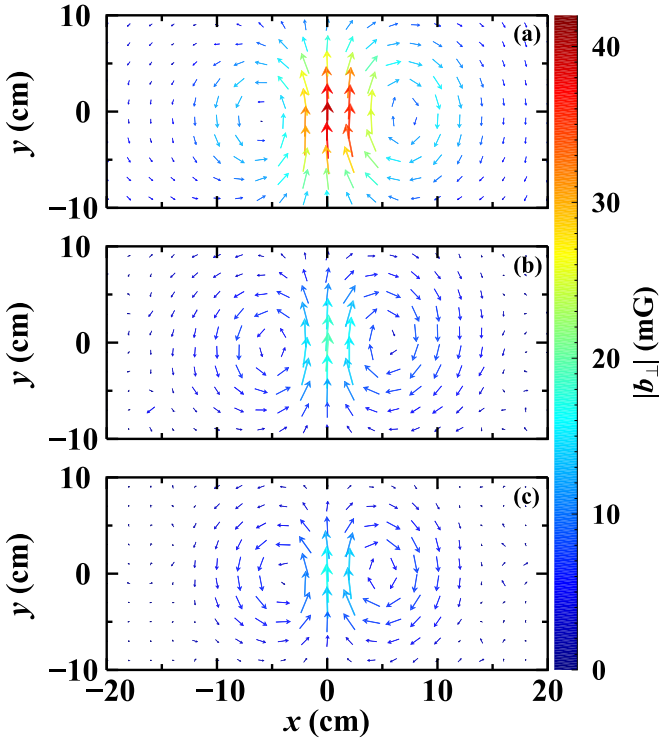

Figure 15. Wave magnetic field in the xy cross section of LAPD (a) before the gradient at $z = z_2$, (b) within the gradient at $z = 8$ m, and (c) after the gradient at $z = z_3$. The direction of the arrows represents that of the wave magnetic field and the colors give the magnitude of the field using the color bar shown. The arrow lengths are normalized by the maximum value of the magnetic field in each panel. For these measurements B_{lo} was 500 G, B_{hi} was 1600 G, and the wave frequency was 76.8 kHz. Note that the x and y spacing of the data points here is 2 cm as opposed to 1.5 cm in Figure 5.

5.2.2. Mode Coupling

The energy of a shear Alfvén wave traveling through a v_A gradient may decrease if a part of the wave energy is converted into another mode. Inhomogeneity in the magnetic field can enable the propagation of compressible surface magneto-acoustic waves and incompressible surface Alfvén waves (Roberts 1981). A gradient in the magnetic field may convert some of the shear Alfvén wave energy to a slow wave (Southwood & Saunders 1985). A fast wave may get excited. All of these modes induce a parallel perturbation, which we have tried to detect using B-dot probes. The ratio $b_\parallel/b_\perp$ was measured before, within, and after the gradient. Mode conversion into these modes would produce an amplification of $b_\parallel$, but we did not detect any $b_\parallel$ above the noise level of ≈0.5 mG. This implies that mode conversion is unlikely.

In order to further confirm that the only mode propagating in the gradient is a shear Alfvén wave, we have measured the wave magnetic fields before, within, and after the gradient. Figures 15(a)–(c) show the structure of the wave before, within, and after the magnetic field gradient, respectively. Two well formed current channels are observed, with the separation between the current channels decreasing in the gradient and on the high-field side, as is expected for shear Alfvén waves propagating along converging magnetic field lines. Considering that we have not detected any wave other than the shear Alfvén wave in the gradient, and that the structure of the shear Alfvén wave within the gradient is consistent with that before and after the gradient, energy reduction due to mode conversion is unlikely.

5.2.3. Nonlinear Effects and Transit-time Damping

Large-amplitude shear Alfvén waves can lose energy due to nonlinear effects. The experiments reported in this paper were carried out using very low-amplitude waves of $b/B_0 \lesssim 8 \times 10^{-5}$. Nonlinear effects associated with shear Alfvén waves, such as parametric instability, have been found to occur only for relatively large-amplitude waves. For example, Dorfman & Carter (2016) reported the threshold for observation of parametric instability of shear Alfvén waves to be $b/B_0 \geqslant 2 \times 10^{-3}$. This is over 10 times greater than our wave amplitude. Low-amplitude shear Alfvén waves also exhibit nonlinear effects in a narrow band of frequencies around the ion cyclotron frequency due to ion cyclotron resonance. As the range of wave frequencies excited here is $\leqslant f_{ci}/2$, nonlinear effects due to ion cyclotron resonance are expected to be absent.

A shear Alfvén wave may exert a mirror force on the electrons and ions, and contribute to additional damping of the wave. This damping mechanism is called transit-time damping. For uniform plasmas with $v_{ti}^2 \ll v_A^2$ and $T_i < T_e$, the mirror force experienced by an electron is greater than that for an ion, and is given by $|F_{Me}| \sim (m_e v_{te}^2/2B_0) k_\parallel b_\parallel$ (Hollweg 1999). In order to estimate the relative importance of transit-time damping with respect to collisional damping, we have compared $|F_{Me}|$ with the frictional force experienced by an electron, $|F_{fric,e}| \sim m_e v_{te} \nu_e$ (Swanson 1989). For our experimental parameters of $n = 2.8 \times 10^{12}\,\mathrm{cm}^{-3}$, neutral pressure of 10^{-4} Torr, $T_e = 4.9$ eV, maximum value for $b_\parallel$ of 0.5 mG, $B_0 = 500$ G, and $k_\parallel = 0.014$ m, the estimated $|F_{Me}|/|F_{fric,e}|$ is $\sim 8 \times 10^{-8}$. This is extremely small, mainly because $b_\parallel/B_0 < 10^{-6}$ in the gradient. Hence, the transit-time damping due to the mirror force is inconsequential when compared to collisional damping and cannot account for the reduction in wave energy.

6. Discussion and Summary

We have studied the reduction in energy of shear Alfvén waves propagating through v_A gradients in a laboratory experiment under conditions scaled to match solar coronal holes. We have experimentally established that λ/L_A is the independent parameter that describes the decrease in energy of shear Alfvén waves passing through v_A gradients. For values of λ/L_A similar to those in coronal holes, the waves are observed to lose energy by a factor of ≈ 5 more than they do when propagating through a plasma without a gradient, where the energy reduction is by a factor of ≈ 2.

In the absence of a magnetic field gradient, we have used a model to show that the wave energy reduction is caused by collisional and Landau damping. Collisions are found to dominate the wave damping, while the contribution of Landau damping is small.

The cause of the additional damping in the presence of a gradient is unknown. We have constrained the cause of this energy reduction in the gradient by ruling out wave reflection, mode coupling, nonlinear effects, and transit-time damping. Landau and collisional damping may reduce the energy of the shear Alfvén wave in the gradient and deposit the wave energy in the plasma. However, a detailed theoretical analysis to accurately determine their contribution using plasma kinetic theory in the non-WKB regime relevant to our experiments is beyond the scope of this paper.

Since the most probable mechanisms that can reduce the energy of the incident shear Alfvén wave without transferring the energy to the plasma do not account for the observed energy reduction, and as the total energy must be conserved, it is likely that the waves deposit their energy in the plasma, thereby contributing to plasma heating or generating a bulk flow. If the total energy lost by the wave contributed to electron heating, then the maximum increase in T_e would be $\sim 23\ \mu$eV. Unfortunately this is too small an increment to measure with a Langmuir probe. If the total wave energy gave rise to a bulk flow, then the flow velocity would be $v_f \sim 0.003\ c_s$, which is too weak to be detected with a Mach probe. The reason for the expected small rise in T_e or weak v_f is due to the low amplitude of the shear Alfvén wave. The energy lost by the shear Alfvén wave is only $\sim 55\ \mu$J. This is a tiny fraction of the ~ 1 J thermal energy of the plasma in the longitudinal gradient. In future experiments we hope to determine the location where the wave energy is being deposited. In order to detect ΔT_e or v_f, we plan to excite large-amplitude shear Alfvén waves and carry out simultaneous T_e and v_f measurements as the wave propagates through the gradient.

The authors thank W. Gekelman for stimulating discussions. This material is based, in part, upon work supported by the U.S. Department of Energy, Office of Science, Office of Fusion Energy Science under Award Number DE-SC-0016602. The experiments were performed at the Basic Plasma Science Facility (BaPSF), which is supported by the DOE and NSF, with major facility instrumentation developed via an NSF award AGS–9724366.

ORCID iDs

Sayak Bose https://orcid.org/0000-0001-8093-9322
Troy Carter https://orcid.org/0000-0002-5741-0495
Michael Hahn https://orcid.org/0000-0001-7748-4179
Shreekrishna Tripathi https://orcid.org/0000-0002-6500-2272
Stephen Vincena https://orcid.org/0000-0002-6468-5710
Daniel Wolf Savin https://orcid.org/0000-0002-1111-6610

References

Alfvén, H. 1942, Natur, 150, 405
Baille, P., Chang, J.-S., Claude, A., et al. 1981, JPhB, 14, 1485
Bemporad, A., & Abbo, L. 2012, ApJ, 751, 110
Braginskii, S. I. 1965, in Review of Plasma Physics, ed. M. A. Leontovich (New York: Consultants Bureau)
Breun, R., Brooker, P., & Brouchous, D. 1987, Stabilization of MHD Modes in an Axisymmetric Magnetic Mirror by Applied RF Waves and Initial Results of Phaedrus-B (Vienna: IAEA), http://inis.iaea.org/search/search.aspx?orig_q=RN:18091939
Campos, L. 1988, JPhA, 21, 2911
Churchill, R., & Brown, J. 1987, Fourier Series and Boundary Value Problems (4th ed.; New York: McGraw-Hill)
Cramer, N. 2001, The Physics of Alfvén Waves (Berlin: Wiley-VCF)
Cranmer, S. R. 2002, SSRv, 101, 229
Cranmer, S. R. 2009, LRSP, 6, 3
Cranmer, S. R., & Van Ballegooijen, A. 2005, ApJS, 156, 265
Cross, R. 1988, An Introduction to Alfvén Waves (Bristol: Adam Hilger)
De Pontieu, B., Carlsson, M., van der Voort, L. R., et al. 2012, ApJL, 752, L12
Dmitruk, P., Milano, L. J., & Matthaeus, W. H. 2001, ApJ, 548, 482
Dorfman, S., & Carter, T. 2016, PhRvL, 116, 195002
Fried, B. D., & Conte, S. D. (ed.) 1961, The Plasma Dispersion Function (New York: Academic)
Gekelman, W., Leneman, D., Maggs, J., & Vincena, S. 1994, PhPl, 1, 3775
Gekelman, W., Pribyl, P., Lucky, Z., et al. 2016, RSciI, 87, 025105
Gekelman, W., Vincena, S., Leneman, D., & Maggs, J. 1997, JGRA, 102, 7225

Gekelman, W., Vincena, S., Van Compernolle, B., et al. 2011, PhPl, 18, 055501
Gigliotti, A., Gekelman, W., Pribyl, P., et al. 2009, PhPl, 16, 092106
Goossens, M., Andries, J., Soler, R., et al. 2012, ApJ, 753, 111
Goossens, M., Terradas, J., Andries, J., Arregui, I., & Ballester, J. 2009, A&A, 503, 213
Gross, E. P. 1951, PhRv, 82, 232
Hahn, M., Landi, E., & Savin, D. W. 2012, ApJ, 753, 36
Hahn, M., & Savin, D. W. 2013, ApJ, 776, 78
Hollweg, J. V. 1999, JGRA, 104, 14811
Hood, A., Ireland, J., & Priest, E. 1997, A&A, 318, 957
Huba, J. & Naval Research Laboratory 2018, NRL Plasma Formulary (Washington, DC: Naval Research Laboratory)
Karavaev, A., Gumerov, N., Papadopoulos, K., et al. 2011, PhPl, 18, 032113
Kletzing, C., Bounds, S., Martin-Hiner, J., Gekelman, W., & Mitchell, C. 2003, PhRvL, 90, 035004
Leneman, D., Gekelman, W., & Maggs, J. 2006, RScI, 77, 015108
Lysak, R. L. 2008, PhPl, 15, 062901
Matthaeus, W. H., Zank, G. P., Oughton, S., Mullan, D. J., & Dmitruk, P. 1999, ApJL, 523, L93
McIntosh, S. W., De Pontieu, B., Carlsson, M., et al. 2011, Natur, 475, 477
Mitchell, C., Maggs, J., Vincena, S., & Gekelman, W. 2002, JGRA, 107, 1469
Moore, R., Suess, S., Musielak, Z., & An, C.-H. 1991a, ApJ, 378, 347
Moore, R. L., Musielak, Z. E., Suess, S. T., & An, C. H. 1991b, in Mechanisms of Chromospheric and Coronal Heating, ed. P. Ulmschneider, E. R. Priest, & R. Rosner (Berlin: Springer), 435
Morales, G., Loritsch, R., & Maggs, J. 1994, PhPl, 1, 3765
Morales, G., & Maggs, J. 1997, PhPl, 4, 4118
Morton, R., Tomczyk, S., & Pinto, R. 2015, NatCo, 6, 7813
Musielak, Z., Fontenla, J., & Moore, R. 1992, PhFlB, 4, 13
Narain, U., & Ulmschneider, P. 1996, SSRv, 75, 453
Ofman, L., & Davila, J. 1995, JGRA, 100, 23413
Oughton, S., Matthaeus, W. H., Dmitruk, P., et al. 2001, ApJ, 551, 565
Perez, J. C., & Chandran, B. D. 2013, ApJ, 776, 124
Priest, E. 2014, Magnetohydrodynamics of the Sun (Cambridge: Cambridge Univ. Press)
Roberts, B. 1981, SoPh, 69, 39
Roberts, D., Hershkowitz, N., Majeski, R., & Edgell, D. 1989, in AIP Conf. Proc 190, Radio-frequency Power in Plasmas (Melville, NY: AIP), 462
Southwood, D., & Saunders, M. 1985, P&SS, 33, 127
Stasiewicz, K., Bellan, P., Chaston, C., et al. 2000, SSRv, 92, 423
Stix, T. 1992, Waves in Plasmas (New York: AIP)
Stix, T. H., & Palladino, R. W. 1958, in Proc. 2nd UN Int. Conf. on the Peaceful Uses of Atomic Energy, ed. J. H. Martens et al. (Herndon, VA: UN Publications), 282
Swanson, D., Clark, R., Korn, P., Robertson, S., & Wharton, C. 1972, PhRvL, 28, 1015
Swanson, D. G. 1989, Plasma Waves (Boston, MA: Academic)
Thuecks, D., Kletzing, C., Skiff, F., Bounds, S., & Vincena, S. 2009, PhPl, 16, 052110
Van Doorsselaere, T., Nakariakov, V., & Verwichte, E. 2008, ApJL, 676, L73
Vincena, S., Gekelman, W., & Maggs, J. 2001, PhPl, 8, 3884
Vincena, S. T. 1999, PhD thesis, Univ. California, Los Angeles
Vranjes, J., Petrovic, D., Poedts, S., Kono, M., & Čadež, V. 2006, P&SS, 54, 641
Yasaka, Y., Majeski, R., Browning, J., Hershkowitz, N., & Roberts, D. 1988, NucFu, 28, 1765
Zhang, Y., Heidbrink, W., Boehmer, H., et al. 2008, PhPl, 15, 012103